Chemical Engineering Science 339 (2027) 125192

Contents lists available at ScienceDirect

Chemical Engineering Science

journal homepage: www.elsevier.com/locate/ces

Dispersed fluid flow in a periodic converging-diverging microchannel

Jie Qi [a], Qingrong He [c], Ke Xu [a,b,*]

[a] Peking University, College of Engineering Department of Energy and Resources Engineering, Beijing 100871, China
[b] Peking University, Institute of Energy, Beijing 100871, China
[c] University of Houston, Department of Biomedical Engineering, Houston, TX, USA

ARTICLE INFO

Keywords:
Dispersed fluid flow
Converging–diverging geometry
Microfluidics
Blob transport
Bretherton model

ABSTRACT

Dispersed fluid (emulsion/foam) flow in confined geometries underlies many geological, environmental, biochemical and engineering processes, yet its hydrodynamic behavior remains challenging to predict. Here we experimentally study dispersed fluid flow along a periodic converging–diverging microchannel, mimicking disordered engineering and geological media. When increasing total flux while fixing dispersed phase flux and blob volume, we observe non-monotonic response of pressure drop with three regimes identified: 1) dense packing of blobs conforming to the confinement at high dispersed phase volume fraction, S_d, 2) intermittent contacting blobs flowing along centerline of the channel at intermediate S_d, and 3) independent blob migration at low S_d. The classic Bretherton model fails to capture the first regime. We rationalize this failure of the Bretherton model and identify the breakdown of two key assumptions: S_d no longer linearly changes with the fractional flow, and the fraction of channel dominated by blob flow is re-modulated by converging–diverging units. We propose a critical modification that well recovers the missing first regime and significantly improves pressure-gradient predictions without additional fitting parameter. These results provide a more general basis for constitutive understanding and utilizing emulsion and foam flow through non-ideal channels and porous media.

1. Introduction

Dispersed fluid flow refers to the flow of discrete droplets, bubbles, cells, or slugs (referred to here collectively as blobs) along with a continuous-phase fluid. As blobs behave as independent microreactors (Zhang et al., 2017; Falk and Commenge, 2010), chemical pockets (Moragues et al., 2023; Sarkar et al., 2024), or flow field control agents (Engl et al., 2005; Zhao et al., 2020), dispersed fluid flow is widely adopted in engineering or natural confined geometries (microchannels, membranes, geological porous media, etc.) for applications such as micro-reactor & micro-extractor design (Thorsen et al., 2001; Yao et al., 2015), chemical sensing (Lu et al., 2020; deMello, 2006), biomedical systems (Paul et al., 2016; Timko et al., 2011), hydrocarbon recovery (Du et al., 2020; Zhang et al., 2025), and geological carbon sequestration (Lei et al., 2025; Ratanpara et al., 2025). In such systems, blobs deform to conform to the geometric confinement (Gai et al., 2022; Raimondi et al., 2014), with distinct flow and rheological behavior from that in open space (Zhang et al., 2025).

Most existing quantitative descriptions of blob transport in confined geometry are developed assuming simple uniform channels with constant cross-section. A classical starting point is Bretherton's analysis in a cylindrical tube (Bretherton, 1961), which shows that, at low Reynolds number (Re) and low capillary number (Ca), the pressure drop along a gas slug scales as $\Delta P_{cap} \propto Ca^{2/3}$. Here, $Re = \rho_c u L/\mu_c$ and $Ca = \mu_c u/\sigma$, where ρ_c and μ_c are the density and dynamic viscosity of the continuous phase, respectively, u is the characteristic flow velocity, L is the characteristic length, and σ is the interfacial tension. Later studies extend this framework to other uniform-channel geometries, while retaining the same basic condition that the cross-section remains constant along the flow direction (Fuerstman et al., 2007; Sheng et al., 2024). In such channels, the dispersed-phase is commonly represented as blobs migrating sequentially along the channel at steady state. Although the detailed expressions differ, these models share the same structure: a viscous contribution from the blob-free liquid region, a viscous contribution from flow around the blob body, and an interfacial contribution from the blob interfaces. In normalized form, they can be written as (Bretherton, 1961; Fuerstman et al., 2007; Mauray et al., 2020):

$$F = Ca(1 - S_d) + aS_dCa + bS_dCa^c \tag{1}$$

here $F = \frac{|\nabla P|}{|\nabla P^*|}$ is the normalized hydraulic resistance, where $|\nabla P^*|$ is the

* Corresponding author.
E-mail address: kexu1989@pku.edu.cn (K. Xu).

https://doi.org/10.1016/j.ces.2026.125192
Received 10 June 2026; Received in revised form 17 August 2026; Accepted 18 September 2026
Available online 19 September 2026
0009-2509/© 2026 Elsevier Ltd. All rights are reserved, including those for text and data mining, AI training, and similar technologies.

reference single-phase pressure gradient corresponding to $Ca = 1$ in the single-phase limit ($S_d = 0$). S_d is the dispersed-phase volume fraction in the channel (dispersed-phase volume/total fluid volume). The parameters a, b, and c are dimensionless model parameters. The classical Bretherton scaling corresponds to $c = 2/3$, whereas all three are typically treated as fitting parameters in generalized applications of Eq. (1) (Bretherton, 1961; Fuerstman et al., 2007; Sheng et al., 2024; Mauray et al., 2020; Sheng et al., 2022). These models have been widely used to describe steady blob transport in uniform channels (Fuerstman et al., 2007; Blunt, 2017).

However, most natural media and a substantial portion of engineering channels for dispersed fluid flow are not uniform, with varying cross-section largely complicating blob dynamics (Gepner and Floryan, 2016). As blobs migrate through sequential converging–diverging geometries, they no longer simply follow the continuous-phase flow but experience repeated squeezing (Chaturvedi and Sharma, 2021; Vavra et al., 2022), stretching, acceleration, deceleration (Liu et al., 2019; Izaguirre and Parsa, 2024), and possible capillary trapping (Xu et al., 2015; He et al., 2019; Hilpert, 2007). This behavior contrasts with the steady, sequential migration assumed in uniform channels with constant cross-section and challenges the direct application of classical uniform-channel models to sequential converging–diverging channels. Recent studies have recorded distinct behaviors of individual blobs or short blob trains (Singla et al., 2024; Malodia et al., 2026; Liang et al., 2021) in non-uniform channels, whereas a general description of multi-blob transport remains lacking. Researchers have to adopt Bretherton framework or empirical models for applications such as emulsion-based mobility control and enhanced oil recovery in porous media (Yu et al., 2019; Romero et al., 2011; Liu et al., 2019).

To address this gap, we conduct visualized microfluidic experiments in a periodic converging–diverging microchannel and examine how blob migration changes with flow conditions. We test whether the classical uniform-channel description (Bretherton model) remains applicable in such non-uniform channels. We then identify the conditions under which it breaks down and clarify the physical origins of this limitation. On this basis, we develop a modification that extends this framework to non-uniform confinement. We aim to provide a general experimental and theoretical basis for modeling dispersed-fluid flow in varying cross-section channels and for extending single-channel descriptions to more complex channel systems, including porous media.

2. Materials and methods

2.1. Chemicals and materials

Fluid system. Oil-in-water emulsion is used as the model fluid system in experiments. We use pentadecane (99% AR, Macklin) as the dispersed-phase fluid, with its viscosity $\mu_d = 3$ cP. The continuous phase is deionized water with 0.5 wt% hexadecyltrimethylammonium bromide (CTAB, Macklin) to stabilize the emulsion, and further dyed with 0.03 wt% methyl blue. The continuous viscosity is $\mu_c = 1$ cP. The interfacial tension between the dispersed-phase and continuous-phase is measured by an interface tensiometer (QBZY-1, Fangrui) as $\sigma = 25.4$ mN/m.

Materials and fabrication of microfluidic chips. Transparent microfluidic chips are fabricated by standard soft lithography using NOA81 (Norland Optical Adhesive 81) as the material in direct contact with the fluids. NOA81 is compatible with organic solvents and stable under surface treatment, and has been widely used in microfluidic applications (Bartolo et al., 2008; Levaché and Bartolo, 2014). Microscopic measurements show that the fabrication error of the NOA81 model is $\Delta w = 2$ μm, consistent with previous reports (Huang et al., 2025). In our experiments, the NOA81 surface is treated by UV curing and oxygen plasma to make it hydrophilic (Zhao et al., 2016); with a static water contact angle of $\theta = 10^\circ$.

2.2. Microfluidic design

We design a microfluidic chip to investigate dispersed fluid flow through a single converging–diverging channel. The model is placed horizontally so that gravitational effects can be neglected. The experimental system is shown in Fig. 1a.

Dispersed fluid flow generator. A blob-generation unit is placed upstream to provide the desired dispersed flow in the microfluidic chip (Fig. 1b). In a fixed geometry, the flow is determined by three independent variables: blob volume V_b, dispersed-phase flow rate Q_d, and continuous-phase flow rate Q_c. We therefore use three injectors to control these quantities independently. Injector 1 supplies the dispersed-phase and sets Q_d. Injector 2 supplies the first continuous-phase stream and forms a T-junction with Injector 1; at fixed Q_d, adjusting this flow rate controls blob volume (Fuerstman et al., 2007; Xu et al., 2008; De Menech et al., 2008; Wehking et al., 2013). Injector 3 supplies or withdraws the second continuous-phase stream and thereby sets Q_c. Inlet 3 is connected to the main channel through a two-dimensional membrane that prevents blobs from passing through or breaking up. The flow rates at Inlets 1, 2, and 3 are controlled by syringe pumps (Harvard Apparatus, PhD Ultra, USA). In all experiments, the blob volume is fixed to be slightly larger than the constriction width, which is a typical condition for stable dispersed-fluid flow in complex systems (Yu et al., 2017; Xu et al., 2017; Yu et al., 2018).

The continuous-phase flux is characterized by the apparent flow velocity $u_c = Q_c/A$, and the dispersed-phase flux $u_d = Q_d/A$, where $A = 4 \times 10^{-8}$ m^2 is the average cross-sectional area of the channel. We then recast the flow rates into three dimensionless variables: the total capillary number $Ca = \mu_c(u_c + u_d)/\sigma$, the dispersed-phase flow fraction $f_d = u_d/(u_d + u_c)$, and dispersed-phase capillary number $Ca_d = f_d Ca$. We perform repeated experiments at multiple fixed Ca_d values spanning 10^{-6} to 10^{-4}, with Ca varied from 10^{-6} to 10^{-3}. Further experimental details are provided in *Supplementary Information*.

Converging-diverging single-channel micromodel. The single-channel microfluidic model consists of 100 sequential converging–diverging units, each comprising a wider section (pore body, $d_{pore} = 0.8$ mm) and a narrower section (throat, $w_{throat} = 0.2$ mm). The length of a repeating unit is 1 mm, as shown in Fig. 1c&d.

Pressure drop measurement. A pressure sensor (Fluigent EIPS345, accuracy 0.6%) is installed in conduit 4 between the flow generator and the main channel to measure the pressure drop and calculate the pressure gradient along the channel. A representative measurement procedure is shown in Fig. 1e. The system is considered to reach steady state once the time-averaged pressure drop remains stable for at least 5 min; image recording and pressure acquisition are then performed. During each experiment, we measure the pressure-gradient magnitude and define the normalized hydraulic resistance as $F = \frac{|\nabla P|}{|\nabla P^*|}$. All experiments remain at low Reynolds number ($Re = 0.02$–1.38), so inertial effects are negligible (Chen et al., 2022).

2.3. Image analysis

A 4 K camera (HC-X1500GK, Panasonic) combined with an LED light panel is used to capture the flow behavior. Pressure data are collected and analyzed with a data acquisition system. Movies of the entire channel are recorded after the flow reaches steady state. Each frame is converted to a binary image to identify blobs, continuous-phase, and solid posts. The dispersed-phase volume fraction S_d is evaluated with Image J. Representative single-blob kinematics are then extracted from manually masked image sequences to obtain blob centroid positions and interfacial perimeters over time (see *Supplementary Movie S4*).

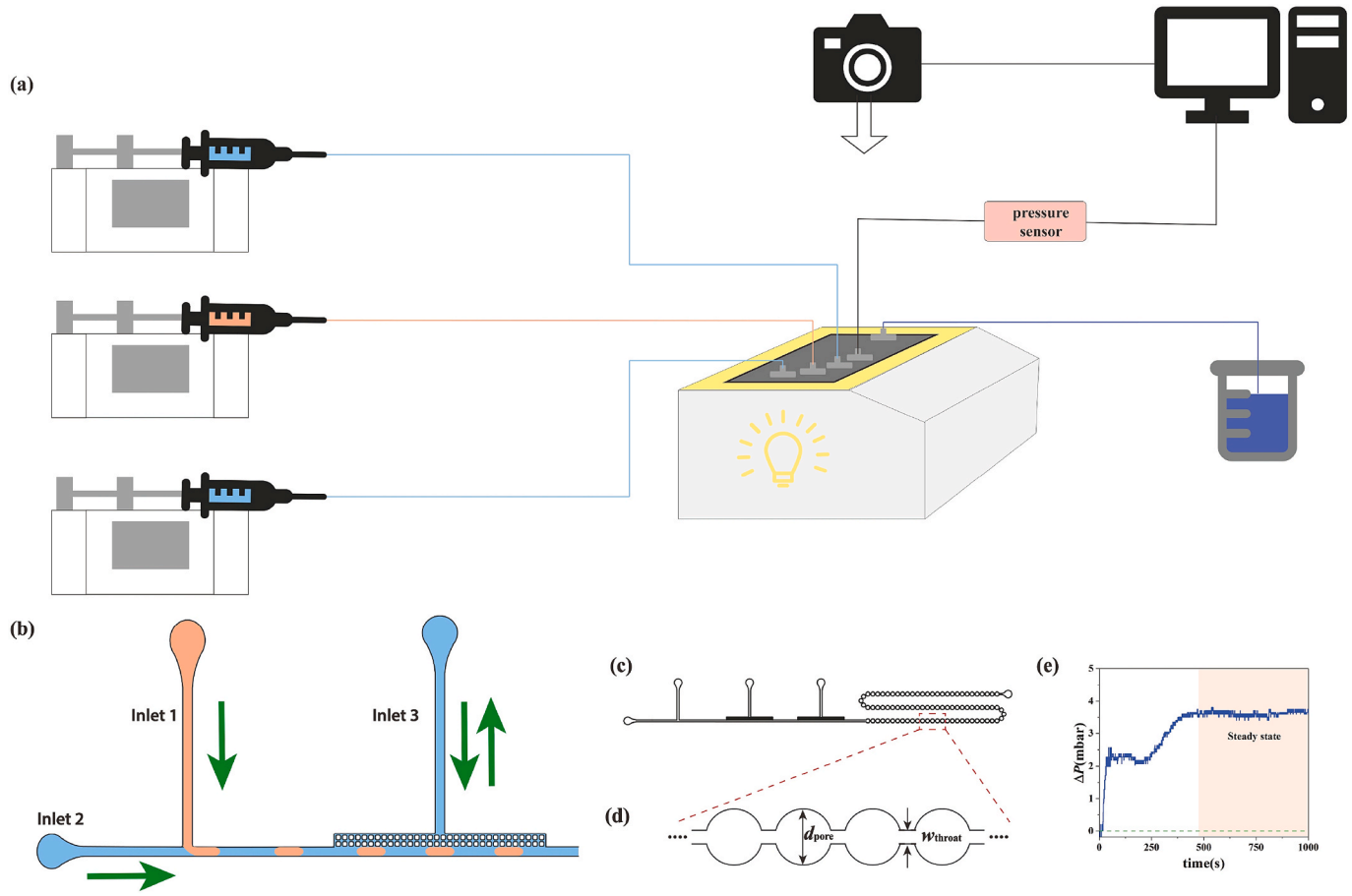

Fig. 1. (a) Schematic diagram of the microfluidic system. (b) Design of the dispersed fluid generator; (c) The whole channel chip structure contains 100 periodic converging–diverging units; (d) Channel geometry design; (e) Representative pressure-drop measurement trace. The green dashed line marks the sensor-zero reference ($\Delta P = 0$ mbar), and the shaded region denotes the steady-state averaging window used to determine the pressure drop.

3. Results and discussion

3.1. Non-monotonic hydraulic-resistance variation and blob-motion characteristics

At fixed blob volume and dispersed-phase capillary number Ca_d, we vary the total capillary number Ca by adjusting continuous-phase flow rate and record the pressure drop and flow images. Surprisingly, the hydraulic resistance (characterized by normalized resistance F) does not monotonically increase with increasing Ca. Instead, as shown in Fig. 2a, the F-Ca curve follows a non-monotonic shape with three segments (increase–decrease-increase). Blob contact and motion modes are very different in three segments, as shown in Fig. 2b. We therefore denote the three segments as Regimes 1–3.

To quantify flow patterns in three regimes, we examine four key characteristics in representative cases of $Ca_d = 8.3 \times 10^{-5}$ (see *Supplementary Movie S1-3*): 1) the isolated-blob fraction, φ_{ind}, defined as the fraction of blobs without direct contact with neighboring blobs; 2) the velocity ratio, U_c/U_d, where $U_c = Q_c/[A(1\text{-}S_d)]$ is the estimated continuous-phase velocity and $U_d = \Delta x/\Delta t$ is measured by blob tracking; 3) temporal evolution of the centroid transverse position, y_c, for tracked blobs; and 4) normalized interfacial perimeter, $\mathscr{P}^*$, for the same blobs (Fig. 2c-e). Fluctuation amplitudes of y_c and $\mathscr{P}^*$ are adopted to characterize the strength of lateral motion and interfacial deformation (Fig. 2f). Flow behaviors in three regimes are summarized as follows:

- Regime 1 (I): low Ca and high S_d. Blobs are largely deformed, in direct contact with the channel wall and with each other so $\varphi_{ind} \approx 0$. $U_c \gg U_d$, showing that the crowded blobs migrate much more slowly than the continuous phase. Both y_c and $\mathscr{P}^*$ show large fluctuation amplitudes, indicating strong transverse motion and large interfacial deformation.
- Regime 2 (II): intermediate Ca and intermediate S_d. Blob contacts become intermittent, and φ_{ind} increases rapidly with Ca from zero to nearly unity. U_c/U_d decreases quickly with Ca from around 10 to 3. Fluctuations in y_c become negligible, showing that blob centroids migrate close to the channel centerline. Fluctuations in $\mathscr{P}^*$ are smaller than in Regime 1, indicating weakened interfacial deformation.
- Regime 3 (III): high Ca and low S_d. Blobs are separated from neighboring blobs (φ_{ind} approaches unity). U_c/U_d decreases much more slowly than that in Regime 2, but remains above unity. Each blob can pass through the throat without direct pushing from the adjacent upstream blob. Fluctuations in y_c and $\mathscr{P}^*$ are both slightly smaller than in Regime 2, similar to that in straight and uniform channels as described by Bretherton-type models.

3.2. Missing Regime 1 in Bretherton-type models

We examine whether the classical uniform-channel model can capture the observed F-Ca variation using its simplest Bretherton framework. In classic Bretherton framework, the interfacial term follows the classical scaling $\Delta P_{cap} \propto Ca^{2/3}$, and the standard uniform-channel closure $S_d = f_d$. Equation (1) then reduces to:

$$F = Ca(1 - f_d) + af_dCa + bf_dCa^{2/3} \tag{2}$$

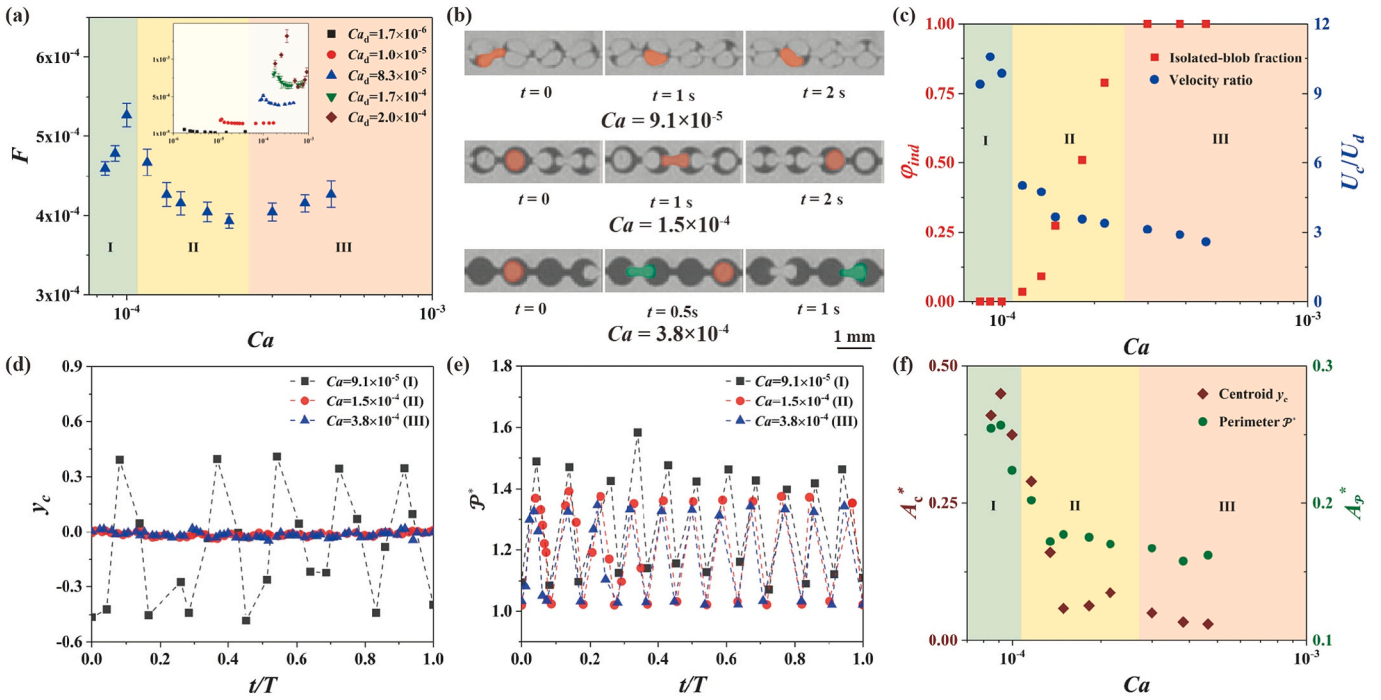

Fig. 2. (a) Typical experimental *F-Ca* curve for a single channel; colors mark Regimes 1–3 at $Ca_d = 8.3 \times 10^{-5}$. Inset: the same non-monotonic pattern persists across the explored Ca_d range (1.7×10^{-6} to 2.0×10^{-4}), sharing the same physical axes of F and Ca as the main panel without repeated axis labels; (b) Representative snapshots of blob transport at three Ca values for $Ca_d = 8.3 \times 10^{-5}$. The red and green circles mark two neighboring blobs; (c) Isolated-blob fraction φ_{ind} and velocity ratio U_c/U_d as a function of Ca at $Ca_d = 8.3 \times 10^{-5}$; (d) Time evolution of the centroid transverse position y_c for the representative blobs in panel (b); (e) Time evolution of the normalized interfacial perimeter $\mathscr{P}^*$ for the same blobs; (f) Centroid oscillation amplitude $A_c^* = (y_{cmax}-y_{cmin})/2$ and perimeter amplitude $A_{\mathscr{P}}^* = (\mathscr{P}^*_{max} - \mathscr{P}^*_{min})/2$ as functions of Ca.

At fixed Ca_d, substituting $f_d = Ca_d/Ca$ into Eq. (2) gives:

$$\left.\frac{\partial F}{\partial Ca}\right|_{Ca_d} = 1 - \frac{b}{3} Ca_d Ca^{-\frac{4}{3}} \tag{3}$$

Eq. (3) implies a two-regime or monotonic behavior of *F-Ca* correlation. The term $(b/3)Ca_d Ca^{-4/3}$ changes monotonically with Ca, which can be much larger than unity at low Ca limit while approximates to zero at high Ca limit. As a result, *F-Ca* curve is descending when $Ca < Ca_c = \left(\frac{b}{3}Ca_d\right)^{\frac{3}{4}}$, and is ascending when $Ca > Ca_c = \left(\frac{b}{3}Ca_d\right)^{\frac{3}{4}}$. Equation (2) therefore can only predict Regimes 2 and 3 qualitatively, with Regime 1 absent.

We fit Eq. (2) against the full dataset, which gives $a \approx 0$ and $b = 0.22$. The comparison between experimental data and the fitted curve is shown in Fig. 3a. Quantitative discrepancies remain between the predicted and measured F values (Fig. 3a), with Regime 1 missing completely. The turning points between Regime 2 and 3 predicted by Eq.

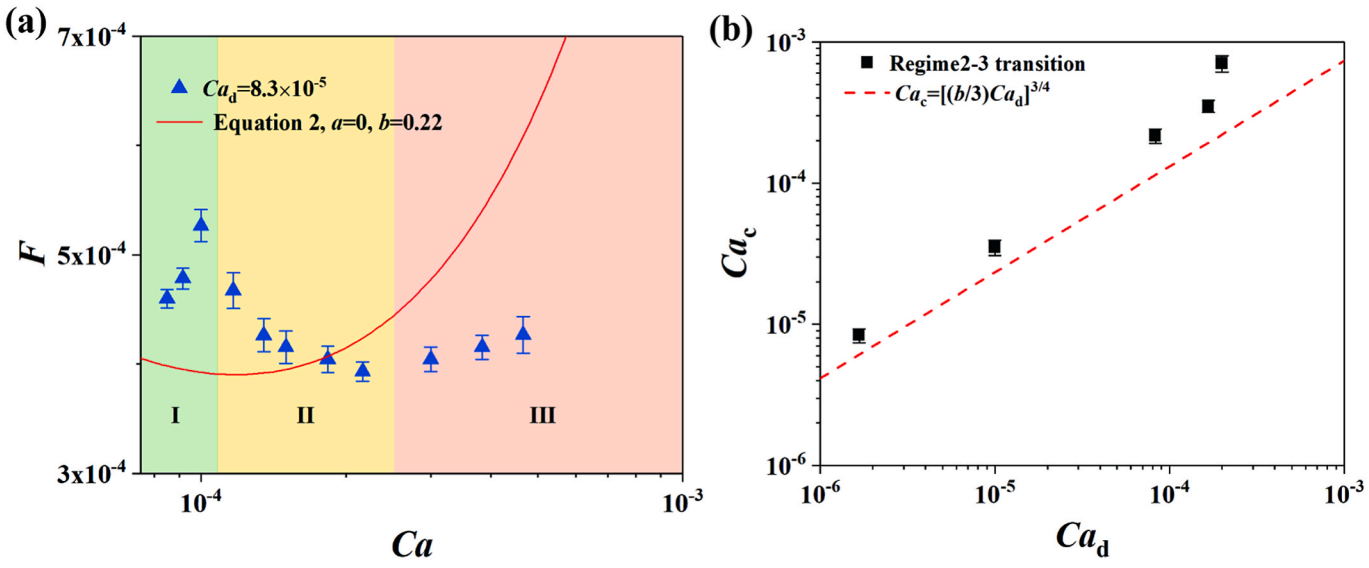

Fig. 3. (a) Experimental *F-Ca* data (blue symbols) and the representative prediction of Eq. (2) (red line) at $Ca_d = 8.3 \times 10^{-5}$, calculated using the globally fitted parameters $a \approx 0$ and $b = 0.22$; (b) Comparison between the predicted Regime 2–3 transition and the experimentally extracted Regime 2–3 transition points.

(3) ($Ca_c = \left(\frac{b}{3}Ca_d\right)^{\frac{3}{4}}$) is systematically lower Ca than the experimentally identified Regime 2 to 3 transitions (Fig. 3b).

In summary, classic Bretherton framework can only qualitatively predict Regime 2 and 3 with major quantitative discrepancy, while cannot rationalize the existence of Regime 1 in a non-uniform channel.

3.3. Modification of Bretherton model

In this subsection, we explore a physically sound modification of the Bretherton model to capture the emergence of Regime 1 and to better capture the flow resistance in all regimes.

The first modification is on the S_d - f_d correlation. In channels with varying cross-section, capillary barriers impose additional resistance on blobs and alter their migration relative to the continuous phase (Mauray et al., 2020; Xu et al., 2015; Perazzo et al., 2018). The uniform-channel relation $S_d \propto f_d$ may therefore break down, particularly in Regime 1. As shown in Fig. 4a, $S_d \sim f_d$ is a reasonable approximation only for $f_d < 0.6$, while S_d stays within a narrow range at higher f_d regime (Regime 1). We project all experimental points onto a f_d - Ca plane and reconstruct the S_d surface using Gaussian process regression (Fig. 4b). It further shows that contours of constant S_d become strongly inclined in high-S_d segment, revealing the high-S_d segment associated with Regime 1.

By adopting $S_d \to 1$ and $dS_d/dCa \to 0$, Eq. (1) can be re-written as $F \approx aCa + bCa^c$ increasing with Ca at fixed Ca_d. This well reproduces the ascending segment of Regime 1.

In addition, the viscous term in Eq. (1) also needs modification. In Eq. (1), the viscous contribution is linear in Ca and partitioned between two liquid regions: blob-free liquid segments, represented by (1-S_d), and bypass flow along the blob-body region, represented by aS_d. This partition is suitable for long slugs in uniform channels, where a blob affects a segment approximately of its own length. However, in a sequential converging–diverging channel or in a typical porous medium, each blob can influence an entire pore–throat unit rather than only the volume it occupies, as shown in Fig. 4c. We therefore recalibrate the viscous term based on the fraction of pore–throat units unaffected by blobs. Since S_d is the blob volume fraction, the affected fraction is estimated as mS_d, where $m = V_u/V_b$ is the ratio of the pore–throat unit volume to the blob volume. The unaffected fraction contributing the blob-free viscous term is therefore $G(S_d) = [1\text{-}mS_d]_+$, with $[x]_+ = \max(x,0)$. The pressure contribution from blob-affected units is represented by the existing interfacial term bS_dCa^c, so the modified model is:

$$F = Ca[1 - mS_d]_+ + bS_dCa^c \tag{4}$$

where $m = 2.69$ in this work which is determined independently from the measured pore–throat and blob volumes. When $Ca \gg Ca_d$ and $S_d = f_d$, $[1 - mS_d]_+ > 0$, Eq. (4) converges to the classic Bretherton framework of Eq. (1). We fit the full experimental dataset with Eqs. (1) and (4) for comparison.

Fig. 5a compares results of three fits methods: (i) Eq. (1) adopting $S_d = f_d$, fitting a, b and c ($R^2 = 0.79$); (ii) Eq. (1) adopting measured S_d, fitting a, b and c ($R^2 = 0.84$); and (iii) Eq. (4) with the measured S_d and $m = 2.69$, fitting only b and c ($R^2 = 0.97$). The third method (Eq.(4)) provides the best overall agreement despite using even fewer adjustable parameters than classic Bretherton framework. Its fitted exponent ($c \approx 0.57$) remains close to the Bretherton exponent of 2/3.

We further test this modified model with data from multiple literature with F ranging over two orders of magnitude (Romero et al., 2011; Mandal and Bera, 2015; Guillen et al., 2012), as shown in Fig. 5b. The model prediction and experimental data well match within the ± 20% error band (detailed derivations are provided in the *Supplementary Information*). It shows that the model improvement is not restricted to the present microchannel geometry.

By simply adopting $S_d \to 1$ and $S_d = f_d$, we successfully get good matching to Regime 1 and Regime 2&3, respectively, as shown in Fig. 5c. Major error only occurs around the crossover region. Detailed derivations are provided in the *Supplementary Information*.

We note that the flow patterns of three regimes aligns closely with the occupation mode of pore units by blobs: when each pore unit contains one or zero blob, blob-blob interactions can be neglected, corresponding to Regime 3; when each pore unit contains two or even more blobs, they start to squeeze and deform each other, pushing the system to Regime 1. We therefore can use this simple geometric picture to predict the regime-transition points. The Regime 1–2 transition corresponds to $mS_d \approx 2$, and the Regime 2–3 transition occurs near $mS_d \approx 1$. Using the approximation of $S_d = f_d$, we get $Ca_{I\text{-}II} \approx mCa_d/2$ and $Ca_{II\text{-}III} \approx mCa_d$, which are highly consistent with the measured transitions (Fig. 5d).

Together with the successful reproduction of Regime 1, major improvement of quantification accuracy, and good matching of transition points, the modified model captures both the crowded high-S_d state and the lower-S_d capillary-viscous competition within one framework. It provides a more general constitutive description for dispersed-fluid transport in confined geometries with varying cross-section, with fewer fitting parameters than the classic Bretherton framework.

3.4. Remaining issue and limitations

In the present theoretical derivation, we establish a constitutive relation for hydraulic resistance at a measured S_d; an explicit closure between S_d and f_d in converging–diverging channels is still lacking. The data in Fig. 4 indicate two limiting trends: at low S_d, the relation remains close to $S_d = f_d$, whereas at high S_d, S_d stays on a plateau while f_d continues to change. These observations explain the failure of the classical uniform-channel model and motivate the correction, but they are not

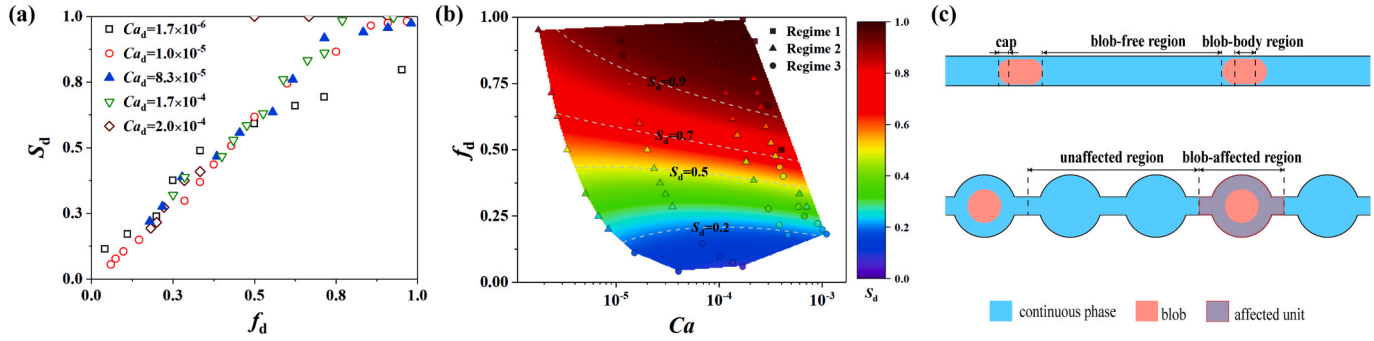

Fig. 4. (a) Measured S_d - f_d data at five fixed Ca_d groups. Filled blue triangles highlight the representative group $Ca_d = 8.3 \times 10^{-5}$; (b) f_d - Ca map colored by S_d. The S_d response surface is reconstructed over the (Ca, f_d) parameter space, superimposed with experimental data points from each flow regime; (c) Schematic comparison of the region affected by one blob: a channel segment approximately equal to the blob length in a uniform channel and an entire pore–throat unit in a converging–diverging channel. The orange region denotes the blob volume V_b, whereas the red overlay denotes the affected unit volume V_u.

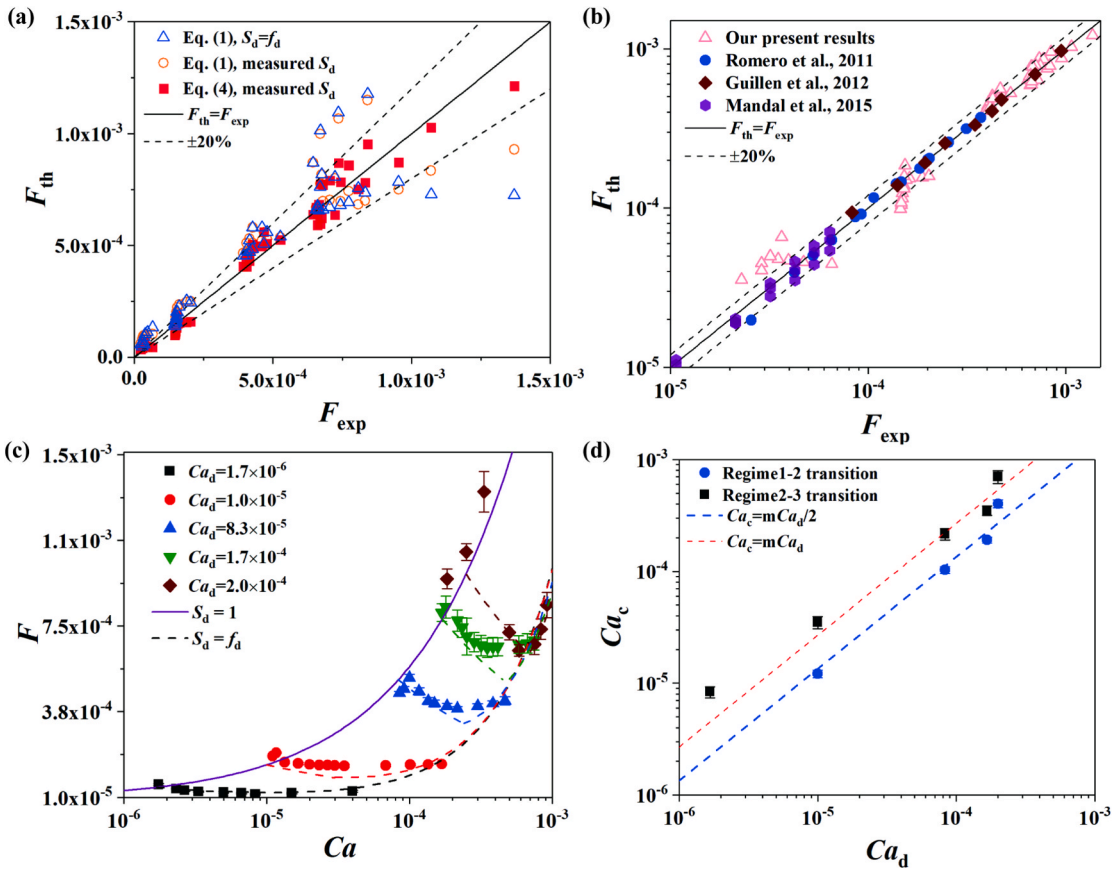

Fig. 5. Validation of the modified model. (a) Comparison between the experimental hydraulic resistance F_{exp} and predictions from the Bretherton model, Eq. (1) and modified model, Eq. (4). Blue open triangles: $a \approx 0$, $b = 0.019$, $c = 0.37$; orange open circles: $a \approx 0$, $b = 0.016$, $c = 0.36$; red filled squares: $b = 0.11$, $c = 0.57$; (b) External comparison using the literature data (Romero et al., 2011; Mandal and Bera, 2015; Guillen et al., 2012). The comparison is performed using $S_d = f_d$ and fitting b and c in the modified model; (c) Reconstruction of the three F-Ca segments using two local limits of Eq. (4): $S_d = 1$ for the high-S_d plateau and $S_d = f_d$ for the low-S_d limit; (d) Comparison of the experimentally identified regime-transition locations with geometry-based estimates. Blue circles and black squares denote the Regime 1–2 and Regime 2–3 transitions, respectively. The dashed lines show $Ca_{I\text{-}II} \approx mCa_d/2$ and $Ca_{II\text{-}III} \approx mCa_d$, respectively, with $m = 2.69$ fixed by geometry.

sufficient to define a general $S_d - f_d$ relation.

In addition, the present work is restricted to a periodic converging–diverging channel with fixed blob volume and simple wettability. It does not address several effects that are important in complex structures, including geometric heterogeneity, blob breakup and coalescence, non-uniform blob volume, wettability, and non-linear interactions within interconnected channel networks. Future work should establish an explicit relation between S_d and f_d for complex structures and determine how this closure depends on geometry and flow conditions, as a next step toward pore-network and representative elementary volume (REV) scale descriptions of dispersed-fluid flow.

4. Conclusion

We experimentally investigate dispersed fluid transport in a periodic converging–diverging microchannel. Within each fixed dispersed-phase flux group and at fixed blob volume, increasing the total flow rate produces a robust non-monotonic variation in hydraulic resistance. We identify three blob transport regimes: a high dispersed-phase volume fraction state with persistent contact between neighboring blobs (Regime 1), an intermediate state with intermittent contact (Regime 2), and a low dispersed-phase volume fraction state with independent blob migration (Regime 3). Classical Bretherton models (Bretherton, 1961; Fuerstman et al., 2007; Sheng et al., 2024) fail to capture Regime 1, whereas they can only qualitatively reproduce the existence Regimes 2 and 3.

We identify that the failure of classic Bretherton framework is due to 1) proportional S_d - f_d relation no longer holds at high S_d condition due to the strong capillarity effect induced by varying blob curvature along converging–diverging geometry, and 2) repeated pore units discretize the volume that a blob can affect. We therefore modify the Bretherton framework and proposes a new model. With one fewer fitting parameter, our new model successfully captures all regimes, reduces the prediction error from ~40% to < 20% over most of the measured range, and accurately predicts the Regime 1–2 and 2–3 transitions. It also reproduces converted literature data for emulsion flow in porous media, with errors generally below 20% (Romero et al., 2011; Mandal and Bera, 2015; Guillen et al., 2012).

These results demonstrate how non-ideal channel geometry may fundamentally alter dispersed-fluid flow behavior by amplifying blob-channel and blob-blob interactions. It provides a more general constitutive basis for dispersed-fluid transport in confined geometry, such as porous media, microfluidic devices, and vascular networks. The modified model is a hydraulic-resistance relation for a measured S_d and the next step is to couple this modified model with explicit S_d - f_d relations and validate it in complex geometries, which would finally bridge the gap between microscopic blob dynamics and channel- or medium-scale flow models.

CRediT authorship contribution statement

Jie Qi: Writing – original draft, Visualization, Investigation, Formal analysis, Data curation. **Qingrong He:** Writing – review & editing, Investigation, Formal analysis. **Ke Xu:** Writing – review & editing,

Supervision, Resources, Project administration, Methodology, Investigation, Funding acquisition, Formal analysis, Data curation, Conceptualization.

Declaration of competing interest

The authors declare that they have no known competing financial interests or personal relationships that could have appeared to influence the work reported in this paper.

Acknowledgements

We gratefully acknowledge the financial support and funding provided by the National Natural Science Foundation of China (Grant No. U23B6004), the National Key Research and Development Program of China (NO. 2023YFA1011700), and by China National Petroleum Corporation-Peking University Strategic Cooperation Project of Fundamental Research. Ke Xu specifically acknowledges very helpful and inspiring discussions with Dr. Matthew Balhoff and Dr. Chun Huh during 2016-2017 when the phenomena were first noticed experimentally.

Appendix A. Supplementary data

Supplementary material: Experimental details, model derivations, transition analysis, external-data comparisons, and videos of blob transport and image analysis. Supplementary data to this article can be found online at https://doi.org/10.1016/j.ces.2026.125192.

Data availability

Data will be made available on request.

References

Bartolo, D., Degré, G., Nghe, P., Studer, V., 2008. Microfluidic stickers. Lab Chip 8 (2), 274–279.
Blunt, M.J., 2017. Multiphase Flow in Permeable Media: A Pore-scale Perspective. Cambridge University Press, Cambridge.
Bretherton, F.P., 1961. The motion of long bubbles in tubes. J. Fluid Mech. 10 (2), 166–188.
Chaturvedi, K.R., Sharma, T., 2021. In-situ formulation of pickering CO2 foam for enhanced oil recovery and improved carbon storage in sandstone formation. Chem. Eng. Sci. 235, 116484.
Chen, L., He, A., Zhao, J., Kang, Q., Li, Z.-Y., Carmeliet, J., Shikazono, N., Tao, W.-Q., 2022. Pore-scale modeling of complex transport phenomena in porous media. Prog. Energy Combust. Sci. 88, 100968.
deMello, A.J., 2006. Control and detection of chemical reactions in microfluidic systems. Nature 442 (7101), 394–402.
De Menech, M., Garstecki, P., Jousse, F., Stone, H.A., 2008. Transition from squeezing to dripping in a microfluidic T-shaped junction. J. Fluid Mech. 595, 141–161.
Du, Y., Mehmani, A., Xu, K., Kelly, S., Balhoff, M., Torres-Verdín, C., 2020. Microfluidic diagnostics of the impact of local microfracture connectivity on hydrocarbon recovery following water injection. Water Resour. Res. 56 (7), e2019WR026944.
Engl, W., Roche, M., Colin, A., Panizza, P., Ajdari, A., 2005. Droplet traffic at a simple junction at low capillary numbers. Phys. Rev. Lett. 95 (20), 208304.
Falk, L., Commenge, J.M., 2010. Performance comparison of micromixers. Chem. Eng. Sci. 65 (1), 405–411.
Fuerstman, M.J., Lai, A., Thurlow, M.E., Shevkoplyas, S.S., Stone, H.A., Whitesides, G.M., 2007. The pressure drop along rectangular microchannels containing bubbles. Lab Chip 7 (11), 1479–1489.
Gai, Y., Montessori, A., Succi, S., Tang, S.K., 2022. Collective behavior of crowded drops in microfluidic systems. Phys. Rev. Fluids 7 (8), 080501.
Gepner, S., Floryan, J., 2016. Flow dynamics and enhanced mixing in a converging–diverging channel. J. Fluid Mech. 807, 167–204.
Guillen, V.R., Romero, M.I., Carvalho, M.D.S., Alvarado, V., 2012. Capillary-driven mobility control in macro emulsion flow in porous media. Int. J. Multiph. Flow 43, 62–65.
He, L., Luo, Z., Bai, B., 2019. Release of a trapped droplet in a single micro pore throat. J. Colloid Interface Sci. 554, 1–8.
Hilpert, M., 2007. Capillarity-induced resonance of blobs in porous media: analytical solutions, Lattice–Boltzmann modeling, and blob mobilization. J. Colloid Interface Sci. 309 (2), 493–504.
Huang, T., Qian, H., Huang, X., Xu, N., Yin, D., Long, Y., Huang, X., Huang, Z., 2025. Effects of porous media geometry and oil repellents on enhanced recovery in water-wet microfluidic chips. Microfluid. Nanofluid. 29 (8), 58.
Izaguirre, M., Parsa, S., 2024. Emergence of preferential flow paths and intermittent dynamics in emulsion transport in porous media. Soft Matter 20 (17), 3585–3592.
Lei, W., Yang, Y., Yang, S., Zhang, G., Poonoosamy, J., Juel, A., Méheust, Y., Bagheri, S., Wang, M., 2025. Advancing sustainable energy solutions with microfluidic porous media. Lab Chip 25 (14), 3374–3410.
Levaché, B., Bartolo, D., 2014. Revisiting the Saffman-Taylor experiment: imbibition patterns and liquid-entrainment transitions. Phys. Rev. Lett. 113 (4), 044501.
Liang, X., Wang, X., Lu, S., Wang, K., Luo, G., 2021. Pressure drop analysis for the droplet break-up flow in a locally constrictive microchannel. Chem. Eng. Sci. 230, 116190.
Liu, C., De Luca, A., Rosso, A., Talon, L., 2019. Darcy's law for yield stress fluids. Phys. Rev. Lett. 122 (24), 245502.
Liu, Z., Li, Y., Luan, H., Gao, W., Guo, Y., Chen, Y., 2019. Pore scale and macroscopic visual displacement of oil-in-water emulsions for enhanced oil recovery. Chem. Eng. Sci. 197, 404–414.
Lu, S.-M., Peng, Y.-Y., Ying, Y.-L., Long, Y.-T., 2020. Electrochemical sensing at a confined space. Anal. Chem. 92 (8), 5621–5644.
Malodia, A., Dhiman, R., Sadasivan, S., John, B., 2026. Effect of obstruction on the dynamics of compound droplets in microchannels. Microfluid. Nanofluid. 30 (7), 51.
Mandal, A., Bera, A., 2015. Modeling of flow of oil-in-water emulsions through porous media. Pet. Sci. 12 (2), 273–281.
Mauray, A., Chabert, M., Bodiguel, H., 2020. Yield stress fluid behavior of foam in porous media. Phys. Rev. Fluids 5 (9).
Moragues, T., Arguijo, D., Beneyton, T., Modavi, C., Simutis, K., Abate, A.R., Baret, J.-C., deMello, A.J., Densmore, D., Griffiths, A.D., 2023. Droplet-based microfluidics. Nat. Rev. Methods Primers 3 (1).
Paul, C.D., Hung, W.-C., Wirtz, D., Konstantopoulos, K., 2016. Engineered models of confined cell migration. Annu. Rev. Biomed. Eng. 18 (1), 159–180.
Perazzo, A., Tomaiuolo, G., Preziosi, V., Guido, S., 2018. Emulsions in porous media: from single droplet behavior to applications for oil recovery. Adv. Colloid Interface Sci. 256, 305–325.
Raimondi, N.D.M., Prat, L., Gourdon, C., Tasselli, J., 2014. Experiments of mass transfer with liquid–liquid slug flow in square microchannels. Chem. Eng. Sci. 105, 169–178.
Ratanpara, A., Li, Y., Kim, M., 2025. A review of microfluidic approaches for carbon capture and storage research. Lab Chip 25 (22), 5705–5746.
Romero, M.I., Carvalho, M.S., Alvarado, V., 2011. Experiments and network model of flow of oil-water emulsion in porous media. Phys. Rev. E 84 (4), 046305.
Sarkar, A., Jones, Z.R., Parashar, M., Druga, E., Akkiraju, A., Conti, S., Krishnamoorthi, P., Nachuri, S., Aman, P., Hashemi, M., Nunn, N., Torelli, M.D., Gilbert, B., Wilson, K.R., Shenderova, O.A., Tanjore, D., Ajoy, A., 2024. High-precision chemical quantum sensing in flowing monodisperse microdroplets. Sci. Adv. 10 (50), eadp4033.
Sheng, L., Chang, Y., Deng, J., Luo, G., 2022. Hydrodynamics and scaling laws of gas–liquid taylor flow in viscous liquids in a microchannel. Ind. Eng. Chem. Res. 61 (28), 10275–10284.
Sheng, L., Chang, Y., Wang, J., Deng, J., Luo, G., 2024. Hydrodynamics of gas–liquid microfluidics: a review. Chem. Eng. Sci. 285, 119563.
Singla, A., Mehul, B., Ray, B., 2024. Droplet dynamics in a constricted microchannel. Chem. Eng. Sci. 300, 120532.
Thorsen, T., Roberts, R.W., Arnold, F.H., Quake, S.R., 2001. Dynamic pattern formation in a vesicle-generating microfluidic device. Phys. Rev. Lett. 86 (18), 4163–4166.
Timko, B.P., Whitehead, K., Gao, W., Kohane, D.S., Farokhzad, O., et al., 2011. Advances in drug delivery. Annu. Rev. Mater. Res. 41, 1–20. https://doi.org/10.1146/annurev-matsci-062910-100359.
Vavra, E., Puerto, M., Bai, C., Ma, K., Mateen, K., Biswal, L., Hirasaki, G., 2022. Measuring in-situ capillary pressure of a flowing foam system in porous media. J. Colloid Interface Sci. 621, 321–330.
Wehking, J.D., Gabany, M., Chew, L., Kumar, R., 2013. Effects of viscosity, interfacial tension, and flow geometry on droplet formation in a microfluidic T-junction. Microfluidics Nanofluidics 16, 441–453.
Xu, J.H., Li, S.W., Tan, J., Luo, G.S., 2008. Correlations of droplet formation in T-junction microfluidic devices: from squeezing to dripping. Microfluid. Nanofluid. 5 (6), 711–717.
Xu, K., Zhu, P., Huh, C., Balhoff, M.T., 2015. Microfluidic investigation of nanoparticles' role in mobilizing trapped oil droplets in porous media. Langmuir 31 (51), 13673–13679.
Xu, K., Liang, T., Zhu, P., Qi, P., Lu, J., Huh, C., Balhoff, M., 2017. A 2.5-D glass micromodel for investigation of multi-phase flow in porous media. Lab Chip 17 (4), 640–646.
Yao, X., Zhang, Y., Du, L., Liu, J., Yao, J., 2015. Review of the applications of microreactors. Renew. Sustain. Energy Rev. 47, 519–539.
Yu, L., Sang, Q., Dong, M., Yuan, Y., 2017. Effects of interfacial tension and droplet size on the plugging performance of oil-in-water emulsions in porous media. Ind. Eng. Chem. Res. 56 (32), 9237–9246.
Yu, L., Dong, M., Ding, B., Yuan, Y., 2018. Emulsification of heavy crude oil in brine and its plugging performance in porous media. Chem. Eng. Sci. 178, 335–347.
Yu, L., Ding, B., Dong, M., Jiang, Q., 2019. A new model of emulsion flow in porous media for conformance control. Fuel 241, 53–64.
Zhang, J., Wang, K., Teixeira, A.R., Jensen, K.F., Luo, G., 2017. Design and scaling up of microchemical systems: a review. Annu. Rev. Chem. Biomol. Eng. 8, 285–305. https://doi.org/10.1146/annurev-chembioeng-060816-101443.
Zhang, B., Zhao, B., Xu, L., Sun, Z., 2025. Contact angle impacts on multiphase displacement in fractured porous media: a microfluidic study. Geophys. Res. Lett. 52 (12), e2025GL115428.

Zhang, W., Du, T., Xu, X., Zhao, X., 2025. Multi-scale rheology for emulsion stability investigation: Bulk-, interfacial-, and micro-perspectives. Adv. Colloid Interface Sci. 345, 103627.
Zhao, B., MacMinn, C.W., Juanes, R., 2016. Wettability control on multiphase flow in patterned microfluidics. PNAS 113 (37), 10251–10256.
Zhao, X., Feng, Y., Liao, G., Liu, W., 2020. Visualizing in-situ emulsification in porous media during surfactant flooding: a microfluidic study. J. Colloid Interface Sci. 578, 629–640.